Towards the Calibration of the HETGS Effective Area

D. Dewey, K.A. Flanagan, H.L. Marshall, C. Baluta, C.R. Canizares, D.S. Davis, J.E. Davis, T.T. Fang, D.P. Huenemoerder, J.H. Kastner, N.S. Schulz, and M.W. Wise

Center for Space Research
M.I.T.
Cambridge, MA 02139

J.J. Drake, J.Z. Juda, and M. Juda

Harvard-Smithsonian Center for Astrophysics
Cambridge, MA 02139

A.C. Brinkman, C.J.Th. Gunsing, and J.S. Kaastra

Space Research Organization of the Netherlands
Sorbonnelaan 1, 3584 CA Utrecht the Netherlands

G. Hartner and P. Predehl

Max-Planck-Institut für extraterrestrische Physik
Box 1603
D-85740 Garching Germany

ABSTRACT

The High-Energy Transmission Grating for AXAF was tested with the AXAF High Resolution Mirror Assembly during December 1996 through April 1997 at NASA's MSFC X-Ray Calibration Facility. This first-use of the HETG confirms sub-assembly measurements and demonstrates the power of this AXAF grating spectrometer.

This paper discusses calibration goals, summarizes the pre-XRCF performance predictions, describes the XRCF data taken, and outlines the general approach to their analysis—concentrating on the the HETG contribution to the HETGS effective area. Very preliminary examples of the analysis of the XRCF data are presented. At a crude level ($\approx$ 30%) the data are in agreement with sub-assembly predictions. Future detailed analysis will result in a definitive instrument calibration.

Keywords: AXAF, grating, calibration, X-ray, diffraction

1. INTRODUCTION

The High Energy Transmission Grating (HETG) is one of four Scientific Instruments (SIs) that will operate with the High Resolution Mirror Assembly (HRMA) in NASA's Advanced X-ray Astrophysics Facility (AXAF). Two of the AXAF SIs are imaging detectors at the HRMA focal plane: the AXAF CCD Imaging Spectrometer (ACIS) and the High Resolution Camera (HRC). These detectors each consist of two sub-imagers: an "-I" imager (ACIS-I, HRC-I) of large area and square aspect ratio for imaging applications and an "-S" imager (ACIS-S, HRC-S) with a more rectangular aspect ratio designed for grating readout.

Either of the two grating SIs, HETG or LETG,[1,2] can be inserted into the optical path just behind the HRMA and, through diffraction, deflect the rays by angles roughly proportional to their wavelength. By combining the

Other author information: Send correspondence to D.D.: Email: dd@space.mit.edu; Telephone: 617-253-7244; Fax: 617-253-0861
Up-to-date information available at: **http://space.mit.edu/HETG/xrcf.html**

HRMA's high angular resolution (of order 1 arc second) and the grating's large diffraction angles (as high as 100 arc seconds/Å), the HRMA-grating-detector systems are capable of spectral resolving powers up to $E/dE \approx 1000$ in the AXAF energy band.

The complete flight instrument that will be utilized and must be calibrated is the combination of the HRMA, HETG, and the ACIS-S—the *HETG Spectrometer (HETGS)*. This past December through April all three of these major components were integrated for test at NASA's Marshall Space Flight Center (MSFC) in their X-Ray Calibration Facility (XRCF). Previous to XRCF testing, calibrations could only be performed on sub-pieces of these components, *e.g.*, on single mirror shells, grating facets, or CCD chips.

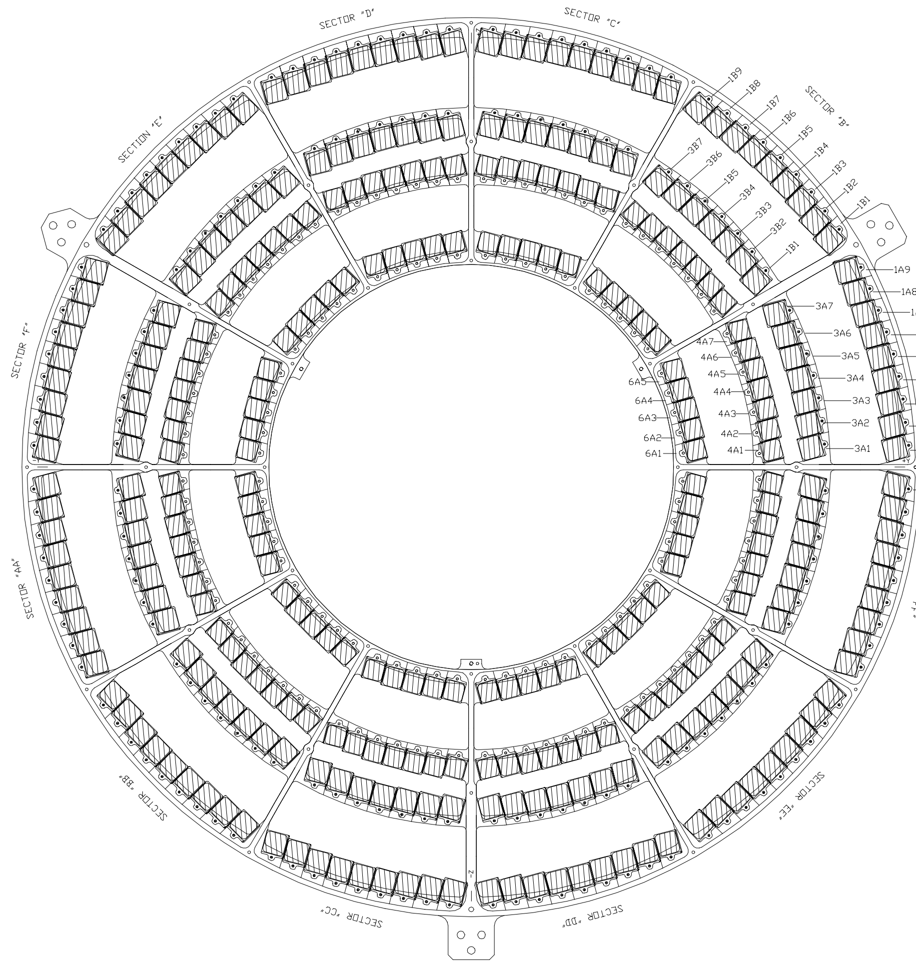

Figure 1. *The HETG. A light-weight ($\approx$ 10 kg) aluminum structure supports 336 individual grating facets in a Rowland geometry. This view of the HETG is from the HRMA side and the facet-location identification scheme is indicated. The HETG, as installed at XRCF, was rotated 180 degrees about the optical axis from this view.*

Details of the HETG have been described previously in these conferences.[3,4] The HETG is a faceted Rowland torus design[5] that has been engineered to place each facet at its prescribed location and orientation on a Rowland torus with Rowland Diameter of 8635 mm. Specifically, in Figure 1 the precision, light weight HETG Element Support Structure[6] (HESS) is populated with 336 individual grating facets. This design combined with the period and period variation properties of the facets allows high resolving powers.

The 336 grating facets of the flight HETG were fabricated in-house at M.I.T. in the Space Microstructures Laboratory (SML) using state-of-the-art holographic lithography techniques.[7] Each facet was then tested in-house for period and diffraction efficiency characteristics.[8]

The four rings of facets on the HETG are designed to intercept and diffract X-rays from the corresponding four HRMA mirror shells. Because most of the high energy area of the HRMA is due to the inner two shells, very fine period (2000 Å) "High Energy Grating" (HEG) facets are used here. The outer two shells have "Medium Energy Grating" facets ("MEG", 4000 Å period) that are efficiency-optimized below 2 keV. These two grating sets have their dispersion axes offset by 10 degrees from each other so that their spectra are spatially separated on the detector. In this way the HETG enables high-resolution spectroscopy ($E/dE > 100$) in the 0.4 keV to 9 keV band.

The HETGS calibration requirements generally fall into two categories: calibration of the *Effective Area* and calibration of the *Line Response Function (LRF).* This paper describes the HETGS effective area calibration; a companion paper[9] focuses on the status of the HETGS LRF calibration.

2. CALIBRATION DEFINITIONS, GOALS, AND PRODUCTS

2.1. Effective Area and Efficiency

The HETGS response to an on-axis monochromatic point source consists of images in the various *diffracted orders* produced at locations given by the grating equation:

$$sin(\theta) = \frac{m\lambda}{p} \tag{1}$$

where m is the order of diffraction (an integer $0, \pm1, \pm2, ...$), p is the grating period and θ is the dispersion angle. Knowledge of the dispersion axis and the grating-to-detector distance, the Rowland distance, allows a conversion of the angle θ to a physical location on the detector.

These diffracted images are, for the most part, spatially localized and so it is possible and convenient to express the system response as the sum of weighted spatial functions:

$$\text{HETGS response}(E, \text{mode}) = \sum_m SEA(E, m, \text{mode}) \times LRF(E, m) \tag{2}$$

where $SEA(E, m, \text{mode})$ is the *system effective area*, described further below, and $LRF(E, m)$ is a unit-normalized line-response function which describes the spatial distribution of the m-th order detected events, see Marshall *et al.*[9] for more details.

The system effective area for the HETGS, in cm^{2}counts/photon, can be calculated from the following terms:

$$SEA(E, m, \text{mode}) = \sum_{s=1,3,4,6} A_s(E)\ \nu_s\ G_s(E, m)\ QE(E, \vec{X}, \text{mode}) \tag{3}$$

Here the sum is over the HRMA mirror shells, A_s is the *optic effective area* for shell s in cm^2, ν_s is a unitless shell-by-shell vignetting factor for the gratings, $G_s(E, m)$ is the average diffraction efficiency for the grating active area on shell s, and $QE(E, \vec{X}, \text{mode})$ is the detector quantum efficiency including effects of detector spatial uniformity ("$\vec{X}$", *e.g.*, BI/FI chips, gaps) and detection mode (*e.g.*, event grading) in counts per photon.

The goal of HETGS calibration is to determine this system effective area for $m = \pm1$ to an absolute accuracy of 10% and a relative accuracy of 3%.[8]

2.2. Fundamental Calibration Products for HETG

The functions $G_s(E, m)$ have sufficient detail for use in modeling the system effective area, however, the LRF functions depend not only on shell-level quantities but on grating-level data, *e.g.*, grating mis-alignment angles.[9] For this reason, the fundamental HETG calibration or model is at the grating level. For each grating facet, $f = 1$ to 336, we have a diffraction efficiency $g_f(E, m)$, period map in facet coordinates $p_f(x, y)$, and alignment distribution $a_f(\phi_{\text{roll}})$ as well as mechanical parameters. These fundamental data can be combined with other information to produce, *e.g.*, $G_s(E, m)$, ν_s, $SEA(E, m, \text{mode})$, and $LRF(E, m)$.

3. PRE-XRCF CALIBRATION ACTIVITIES

3.1. Synchrotron Measurements and Modeling

The key physics to model the HETGS effective area comes in at the level of the single-grating diffraction efficiency $g_f(E, m)$. In order to achieve high diffraction efficiencies, we are operating outside the range of the simple diffraction theory[10] of opaque bars and instead in a region where the grating bars transmit and phase-shift the X-rays. Guided and assisted by Dale Graessle and his AXAF witness mirror work at NSLS,[11] Tom Markert and Christie Nelson initiated grating synchrotron measurements of diffraction efficiency, reported in Nelson *et al.*[12] and Markert *et al.*.[13] These studies have allowed us to verify the phased non-rectangular model, provided reference standards for laboratory tests, and provided more accurate optical constant data for the materials in our gratings. The state of our synchrotron measurements and modelling efforts was most recently detailed by Flanagan *et al.*.[14] Although this work is ongoing, the fundamental result was a detailed physical model of grating diffraction that applies to individual gratings $g_f(E, m)$ and has been measured at many finely spaced energies.

3.2. Sub-assembly Measurement Results

We have been able to determine initial values for the fundamental calibration products for the HETG from laboratory measurements on each grating facet. The basic equipment for HETG grating laboratory testing, a Laser Reflection setup and the X-Ray Grating Evaluation Facility (X-GEF) are described in Dewey *et al.*[8] with more details of the X-GEF facility and its operation for flight testing presented in Flanagan *et al.*.[15] Here we have measured the diffraction efficiency of each flight grating at several energies and orders and fit these measurements to determine the physical-model parameters for each grating. From these best-fit parameters we can generate $g_f(E, m)$ for each grating on a fine energy scale.

The gratings were mounted to the support structure at the HETG Alignment Facility where the average facet roll angle was measured based on the polarization alignment technique of Anderson *et al.*.[16]

We have used these “sub-assembly” data (along with similar predictions for the HRMA and ACIS-S) to produce predicted curves for comparison with the XRCF measurement results.

4. XRCF HARDWARE

The XRCF and related hardware are described in more depth elsewhere in these proceedings, however some key concepts are presented here to support the grating analysis discussion. The general layout of XRCF hardware is shown in Figure 2. Key to effective area measurements are the beam normalization detectors (BNDs) which monitor the source flux without the effects of the HRMA or HETG. There are six BND detectors: two, a Flow Proportional Counter (FPC) and a Ge solid state detector (SSD), are located 37.7 meters from the source in “Building 500”, and four FPCs surround the HRMA entrance. To ensure some BND data is available over a wide range of source flux, apertures can be selected on the FPC_5, SSD_5, and FPC_HN BNDs.

Calibration was divided into two main calibration phases, Phase I and Phase II, defined only by differences in the focal plane detectors—the Beam normalization detectors (BND) were present in both Phases. In Phase I the non-flight detectors, FPC_X2 (Flow Proportional Counter), SSD_X (Solid State Detector), and HSI (micro-channel plate High Speed Imager), were used; in Phase II a “two-chip ACIS” (ACIS-2C) and the flight ACIS and HRC detectors were variously present.

The FPC and SSD are non-imaging detectors with moderate energy resolution and have a variety of apertures used to isolate and measure grating-dispersed spectral features in the focal plane. These detectors have well studied characteristics[17] , are similar to the BNDs, and provide some of the fundamental data for characterizing the efficiencies and effective area of the system without the complication of the flight-detector $QE(E, \vec{X}, \text{mode})$ terms.

The arrangement and operation of the components at XRCF is flight-like with the following differences:

∘ The source is not infinitely far away and so i) the HRMA focal length is greater than the flight value and ii) the HRMA reflection angles and optic illumination are different from flight.
∘ The HRMA is in a “1-g off-loaded” condition approximating the 0-g flight configuration so flight PSFs will be slightly different.

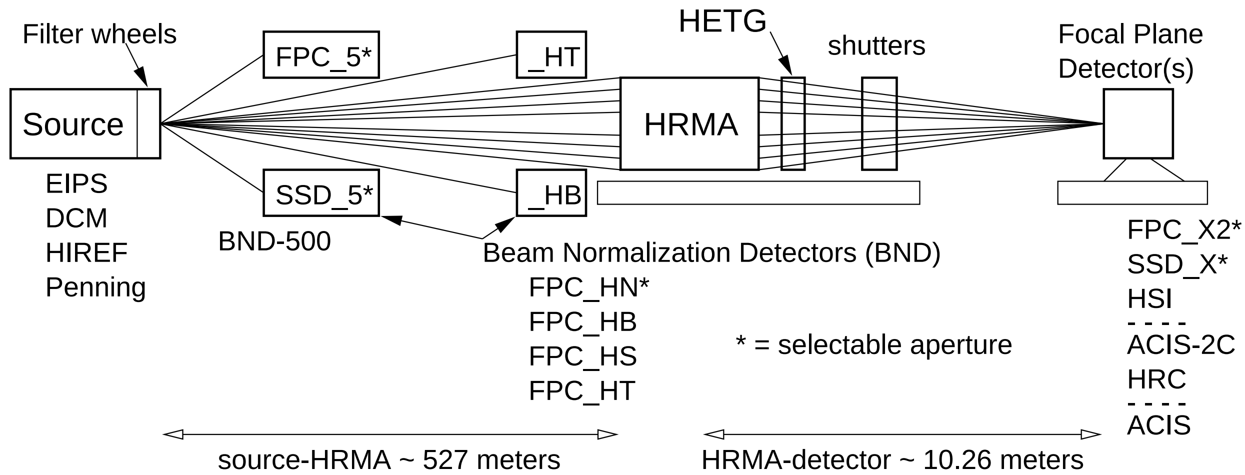

Figure 2. *XRCF hardware schematic. The XRCF HETG configurations include i) X-ray source and filters, ii) Beam normalization detectors (BNDs), iii) AXAF optics (HRMA, HETG), iv) shutter assembly, and v) focal plane detectors.*

∘ The $+Z$ axis of the HRMA and SIs pointed "down" at XRCF, (*i.e.*, aligned to XRCF $-Z$).
∘ The gratings are designed to operate at a Rowland distance of 8635 mm but because of the HRMA focal length change they are placed 8782.8 mm from the focus; this introduces negligible LRF effects and some slight additional vignetting ($< 5\%$).

Some useful XRCF HETG parameters are tabulated in Table 1 for reference.

Table 1. Table of useful XRCF HETG parameters. These preliminary values are based on sub-assembly and XRCF testing.

Description	value	error	units	sub-assembly expectation
Rowland distance	8782.8	0.5	mm	based on XRCF drawings
MEG average period	4000.77	≈ 0.10	Å	LR/NIST: 4001.13±2.00
HEG average period	2000.95	≈ 0.10	Å	LR/NIST: 2000.81±0.05
MEG angle	4.74	0.05	deg.s	CEI spec.: 5.0 ±0.5
HEG angle	−5.19	0.05	deg.s	CEI spec.: −5.0 ±0.5
MEG-HEG angle	9.93	0.01	deg.s	CEI spec.: 10.0 ±0.7

5. XRCF MEASUREMENTS

To support semi-automated test operation, the measurements to be made at XRCF were specified as rows in a 92 column tab-delimited ASCII file. These 92 columns specified nearly completely the desired state of the source, filters, HRMA, gratings, shutters, normalization detectors, and focal plane detectors. Testing proceeded through sequentially "executing" this Calibration Measurement Data Base (CMDB). An as-run (or at least "as-requested"—modifications could be made manually in real time) version of the CMDB is now a useful starting point in understanding what data were taken.

The measurements (rows of the CMDB) were assigned a "measurement type" which both specified a general focal plane hardware operating mode (Phase I in particular) and indicated the scientific purpose of the measurement. Tables 2,3 provide a summary of all data taken at XRCF with the HETG inserted in the optical path and an indication of their use and data volume (number of measurements in brackets.)

The measurement types related to effective area break into two main divisions: *i*) quasi-monochromatic measurements: types EE, 3D(EA), and EA; and *ii*) "Molecular Contamination" (MC) measurements where the broad-band continuum produced by the source is utilized (see the MC example in Section 7.3).

The distinctions between EE, 3D(EA), and EA are primarily in Phase I and represent different methods of placing the focal plane hardware at the desired location: in EE a "beam-center" is performed to set the aperture(s) relative to the reference location specified in the CMDB; in 3D(EA) locations are sampled in the focal plane at specified coordinates from a locations file; and in EA the location is specified in the CMDB.

Finally, a (valuable) fraction of the data were taken while one of the XRCF monochromators was scanned in energy. Although scientifically similar to non-scanned data, these data are more difficult to analyze because there was no direct synchronization between the source scan and the data collection.

Table 2. Table of HETG XRCF Measurements in Phase I. Number of measurements is shown in brackets.

Type	Detector	
	FPC/SSD	HSI
LRF-related . . .		
FC and SF	-	Verify focus, check PSF [16]
dFocus	-	Defocus and in-focus images [2]
Alignment	-	Gross vignetting, mis-aligned gratings [3]
PSF/1D	LRF core, wings [21]	-
PSF/Outer	-	Wings, scatter [8]
3D (Offaxis)	-	Offaxis images [6]
Eff.area-related . . .		
EE	Order locations, effective area [33]	-
3D (EA)	Effective area, high orders [56]	Source spectra, MEG-Penning PSF [32]
EA (fixed E)	Effective area [10]	Source spectra (incl. DCM, HIREF) [9]
EA (mono scan)	Effective area [19]	-
3D (Molecular Contamination)	-	Identify and search for edges, etc. [6]

Table 3. Table of HETG XRCF Measurements in Phase II. Number of measurements is shown in brackets.

Type	Detector		
	ACIS-2C	HRC	ACIS
LRF-related . . .			
FC and SF	Verify/check focus [7]	Verify/check focus [1]	-
dFocus	Find best focus [10]	-	-
PSF/Inner	Core, wings; offaxis images [23]	-	Core, wings; offaxis images [8]
Scattering	Wings, scatter [5]	-	Grating scatter, pileup effects, readout modes (, effective area) [7]
Eff.area-related . . .			
EA (fixed E)	Effective area [133]	Effective area [33]	Effective area [11]
EA (mono scan)	Effective area [29]	Effective area [1]	Effective area [9]
MC (Molecular Contamination)	Identify and search for edges, etc. [53]	-	Identify and search for edges, etc. [5]

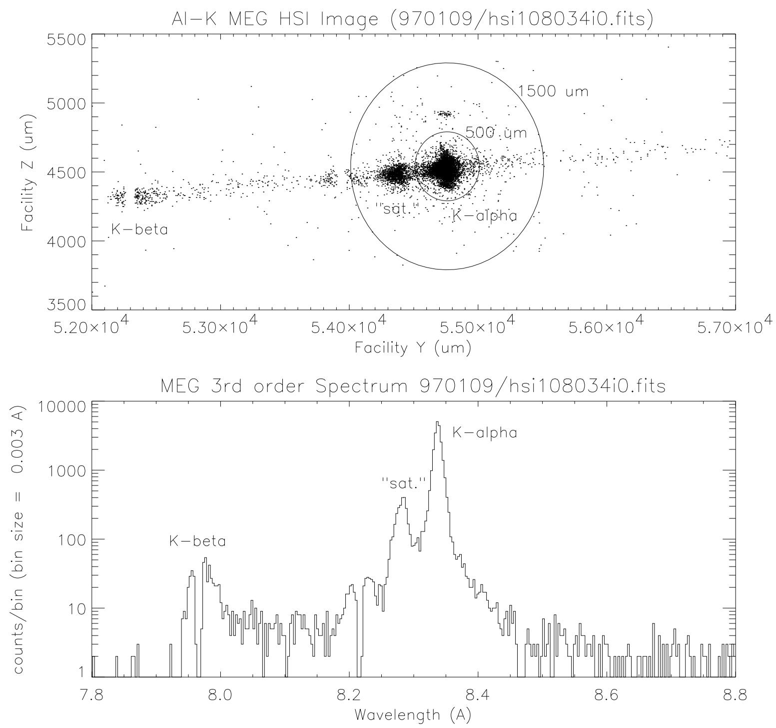

Figure 3. *HSI image of 3rd-order MEG Al-K line (top) and the resulting grating-produced spectrum (bottom). Note that all of this spectral structure is unresolved by the FPC and SSD detectors, Figure 4. A strong "satellite" line is clearly visible near the K-α peak. HSI instrumental gaps have not been removed, e.g., at the K-β line.*

6. EFFECTIVE AREA DATA & ANALYSIS

6.1. Examples of XRCF Data

With complicated data it is best to start with an image—and so in Phase I we generally took images of the diffracted X-rays with the High Speed Imager (HSI). Figure 3 shows the HSI image of the Al-K line in the MEG 3rd order—deflected 55 mm from the zero-order (HRMA focus) location. These are the "raw" HSI data and show the instrumental "gaps",[18] *e.g.*, one goes through the K-β peak. Note that the "line" in fact consists of several discrete lines as well as continuum. The "satellite" line just shortward of the K-α peak has been previously observed during XMM grating testing[19]; we also observe a second, weaker satellite line at 8.22Å.

To accurately measure the intensity of the line in Phase I, the FPC_X2 (or SSD_X) with selected aperture could be moved to the line center and the pulse-height histogram of events through the aperture measured. An example of the acquired focal-plane and BND histograms is shown in Figure 4 for the MEG first order of Al-K and a 500 μm diameter aperture. Note that while the BNDs are able to resolve an Al-K peak and broadband continuum, the detailed spectral structure of the Al-K line is unresolved. The 500 μm first-order aperture size corresponds spectrally to the region within the 1500 μm circle shown in Figure 3—thus the FPC_X2 is detecting the K-α and satellite lines and some continuum, but is excluding other continuun and the K-β peak.

In Phase II the focal plane detectors were all imaging instruments (ACIS-2C, ACIS, and HRC) and so provide their own source spectral diagnostics. Effective area measurements generally did not required precise positioning; in fact, because of per-pixel count-rate limits (set generally by pile-up for ACIS and dose limits for HRC) the measurements were performed with a large defocus. Figure 5 shows an ACIS-2C image of the HEG first-order of Al-K. The defocussed images of the HRMA shells 4 and 6 are modulated by the individual grating facets. Because of the defocus, extraction of the K-α events will necessarily be contaminated by the existence of the other lines and continuum. HRC and ACIS effective area data are very similar to this ACIS-2C example as the ACIS-S event plot of Figure 6 demonstrates.

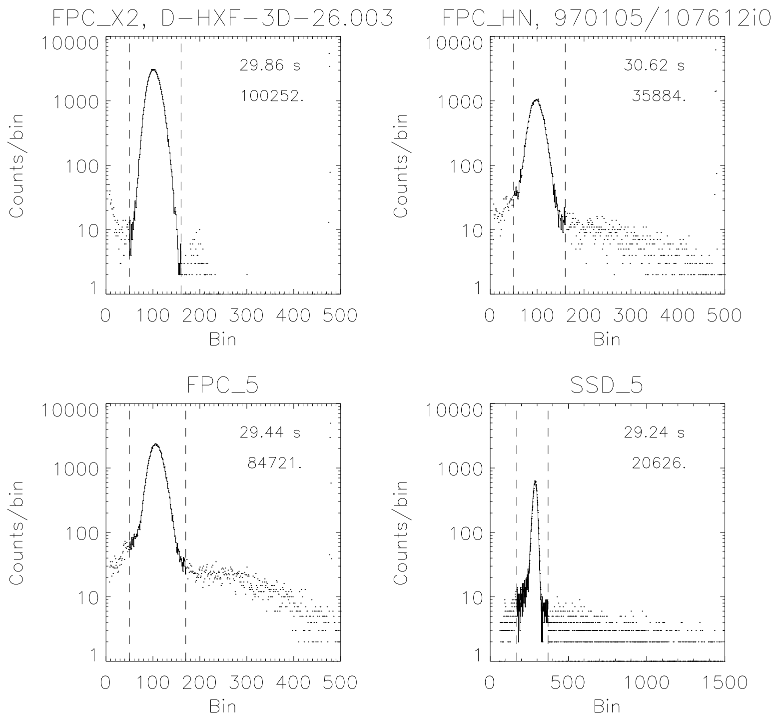

Figure 4. *PHA spectra from Al-K MEG +1 order measurement. The focal plane FPC_X2 shows only a monochromatic response (with a slight pile-up peak at 2E) while the beam normalization detectors (FPC_HN, FPC_5, and SSD_5) show both the Al-K "line" and broad-band (unfiltered) continuum.*

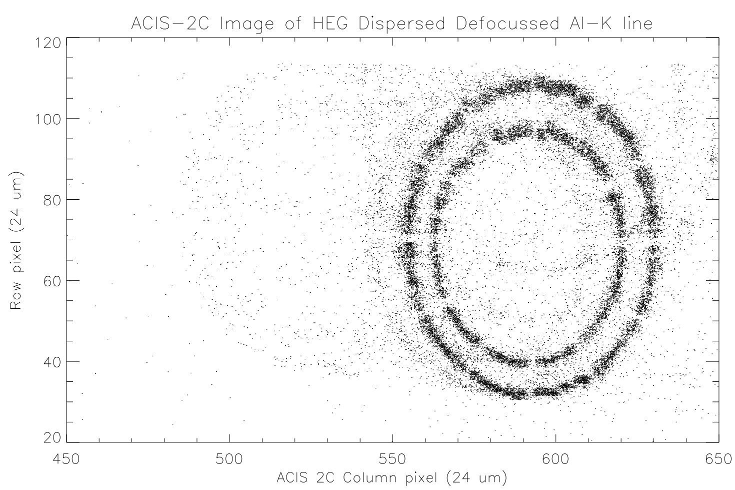

Figure 5. *ACIS-2C defocussed image of HEG dispersed Al-K line. Note that the same line components as in Figure 3 are present.*

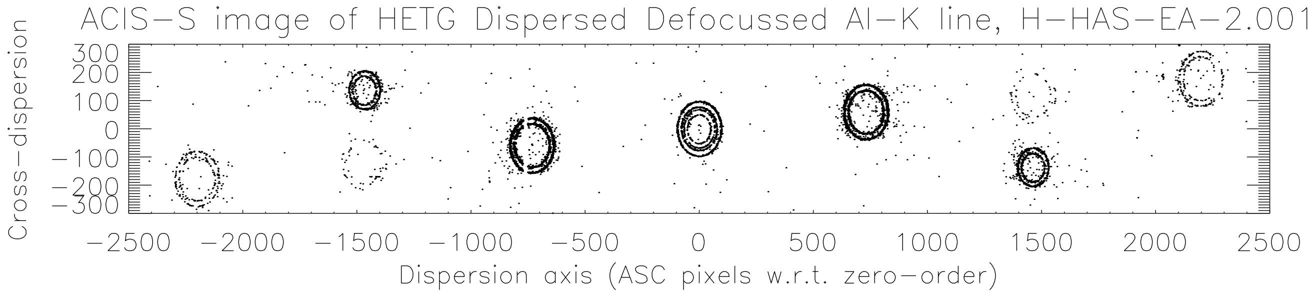

Figure 6. *ACIS-S defocussed image of HETG dispersed Al-K line. The HEG and MEG diffracted orders are clearly identified by the corresponding HRMA shells in their images. For the MEG, orders* $m = \pm 1, \pm 2, \pm 3$ *are visible.*

6.2. Analysis Methods and Equations

The system effective area is calculated from the measurements through the equation:

$$SEA(E_{\text{line}}, m, \text{mode}) = \frac{\text{focal plane counts/s in line order}}{\text{source flux in line}} \quad [\frac{\text{counts/s}}{\text{photons/cm}^2\text{s}} = \text{cm}^2 \frac{\text{counts}}{\text{photon}}] \tag{4}$$

where the units for the quantities are given as well. (Although the terminology "line order" suggests grating applications these considerations apply to HRMA-only measurements as well.) The numerator is derrived from the focal plane data through:

$$\text{focal plane counts/s in line order} = R_{\text{fp}}(\text{mode}) \times L_{\text{fp}}(\text{aperture}, \text{spectrum}, QE_{\text{fp}}) \tag{5}$$

where the focal plane rate $R_{\text{fp}}(\text{mode})$ is the observed count rate in the data—generally this count rate will represent the counts per second within a spatial-spectral "bump" in the data, *e.g.*, the counts in the ROI region of the FPC_X2 spectra. As such this quantity, and others that follow, *has meaning only in the context of a specific analysis method.* The variable "mode" is used here to indicate the additional effect that this rate can depend on the focal plane detector mode of operation, *e.g.*, continous *vs.* timed-exposure modes for ACIS.

The focal-plane line fraction term $L_{\text{fp}}(\text{aperture}, \text{spectrum}, QE_{\text{fp}})$ is a conversion factor from the observed count rate to the count rate that would be due to the line fraction alone. This factor is required because the sources are not truly mono-chromatic and the detectors do not fully separate the line, as indicated in the discussion regarding Figures 4 and 5 above. The line fraction defined here will generally not depend on the detector mode, but *is* taken in the context of an analysis method, *e.g.*, the line fraction will be different if ROI analysis is performed or XSPEC[20] fitting is used.

Note that the SEA as defined here is equivalent to the "total effective area" into 2π and there is an assumption that the line-fraction correction also includes a small correction for the line counts that are outside the aperture. Not discussed here but treated similarly is the *Encircled Effective Area* (often called "Encircled Energy"), *e.g.*, $EEA(E_{\text{line}}, m, \text{mode}, \text{diameter})$ which considers only the counts within the aperture.

The SEA denominator, "source flux in line", is given by:

$$\text{source flux in line} = \frac{R_{\text{BND}} \times L_{\text{BND}}(\text{spectrum}, QE_{\text{BND}})}{QE_{\text{BND}}(E_{\text{line}}) \times A_{\text{BND@HRMA}}} \tag{6}$$

where the BND rate R_{BND} and BND line fraction $L_{\text{BND}}(\text{spectrum}, QE_{\text{BND}})$ are defined analogously to the focal plane terms above. The two additional terms in the denominator provide the key ingredients for the calibration: the BND quantum efficiency $QE_{\text{BND}}(E_{\text{line}})$ provides the conversion from counts to photons for the BND (supporting relative calibration), and the BND area $A_{\text{BND@HRMA}}$ is the equivalent geometric area of the BND detector at the

HRMA aperture and provides the absolute calibration; for the BNDs near the HRMA (*e.g.*, FPC_HN fully open) this value is 32.55 cm^2.

In the calibration of the optical components, the HRMA and HRMA-Gratings, it is useful to consider the *optic effective area (OEA)* which represents the ability of the optical system to collect photons and does not include detector effects:

$$OEA(E_{\mathrm{line}}, m) = \frac{\text{focal plane photons/s in line order}}{\text{source flux in line}} \quad [\frac{\text{photons/s}}{\text{photons/cm}^2\text{s}} = \text{cm}^2] \tag{7}$$

where we get the usual cm^2 units. The OEA may be calculated from the measurements through:

$$OEA(E_{\mathrm{line}}, m) = A_{\mathrm{BND@HRMA}} \times \frac{R_{\mathrm{fp}}(\mathrm{mode}) \times L_{\mathrm{fp}}(\mathrm{aperture, spectrum}, QE_{fp})}{R_{\mathrm{BND}} \times L_{\mathrm{BND}}(\mathrm{spectrum}, QE_{\mathrm{BND}})} \tag{8}$$

$$\times \frac{QE_{\mathrm{BND}}(E_{\mathrm{line}})}{QE_{\mathrm{fp}}(E_{\mathrm{line}}, \mathrm{mode})}. \tag{9}$$

When the focal plane detector has a QE identical to the BND detector the last term is unity and, for non-dispersed orders ($m = 0$ or HRMA-only), the line-fraction corrections are also close to unity. In this way the HRMA effective area can be accurately measured.[21]

7. PRELIMINARY RESULTS

7.1. Phase I Effective Areas

Figures 7 and 8 show the results of an initial analysis of the fixed-energy Phase I optic effective area measurements of the HRMA-HETG in 1st-order and zero-order. A crude region-of-interest analysis (*e.g.*, Figure 4) was performed and a simplified version of the optic effective was calculated:

$$OEA(E_{\mathrm{line}}, m) = A_{BND@HRMA} \times \frac{R_{\mathrm{fp}}}{R_{\mathrm{BND}}} \tag{10}$$

The solid curves here are the combination of the pre-XRCF mirror model with the pre-XRCF HETG efficiency data. Note that the zero-order data is in closer agreement due to its non-dispersive nature.

The 1st-order HRMA-HETG effective area curves can be divided (somewhat arbitrarily) into 5 regions where different physical mechanisms govern the effective area of the optical (mirror-grating) system:

∘ *below 1 keV* – the polyimide membrane of the gratings is dominating the area changes, with edges due to C, N, and O.
∘ *1-2 keV* – the phase effects of the grating cause an increasing enhancement of the diffraction efficiency.
∘ *2-2.5 keV* – edge structure from the mirror (Ir) and grating (Au) dominates, sharply reducing effective area.
∘ *2.5-5.5 keV* – effective area is slowly varying, with some low-amplitude Ir and Au edge structure.
∘ *5.5-10 keV* – the mirror reflectivity and grating efficiency are decreasing rapidly with energy.

Horizontal error bars on the data indicate the corresponding statistical error of the measurement, which is generally below ±5 %. The vertical error lines indicate the probable systematic errors estimated for the 1st-order measurements as +30 % and −10 %. These data illustrate that the absolute effective areas are close to expected values and they show the large range of energies sampled at XRCF.

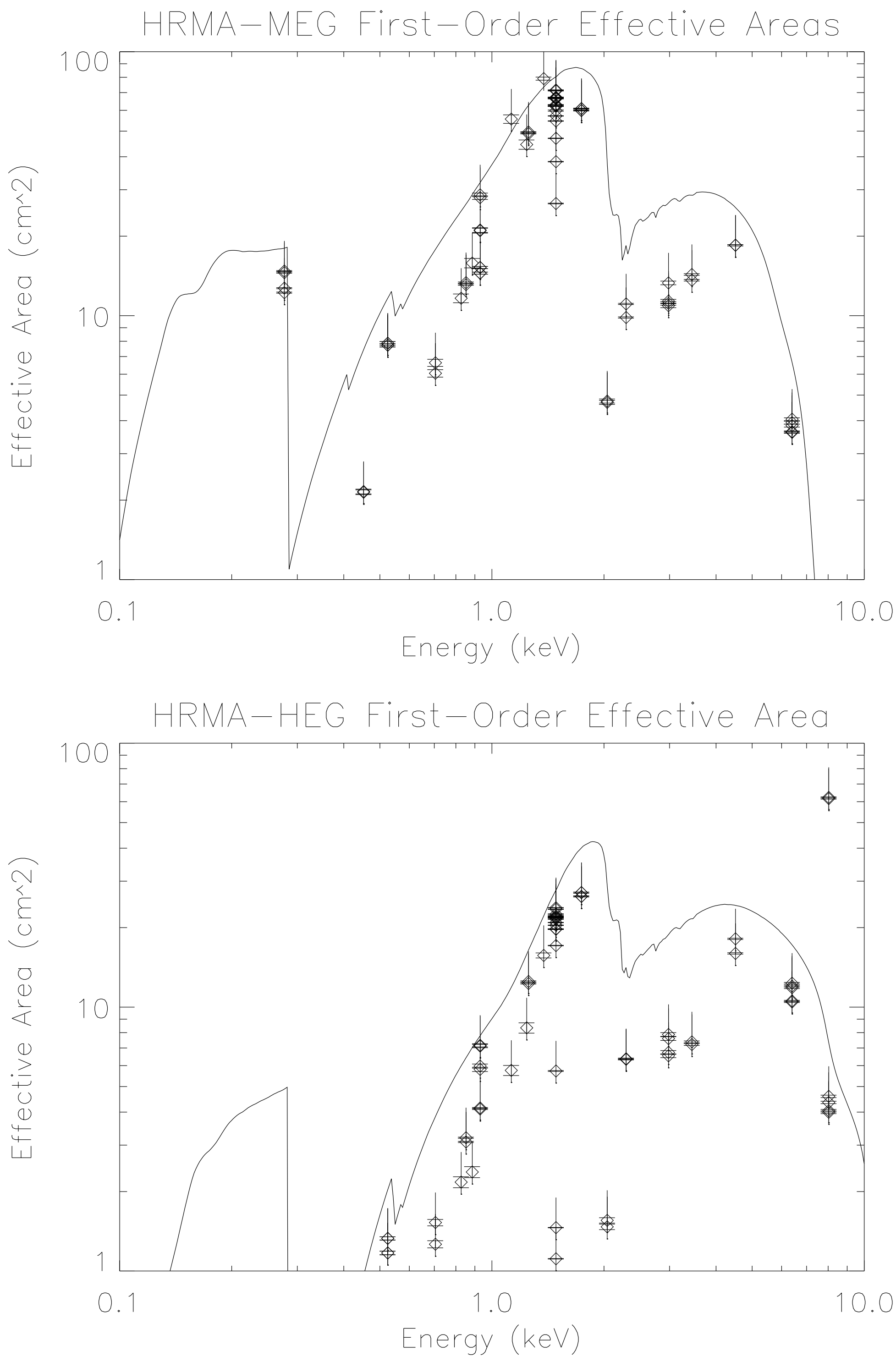

Figure 7. *Preliminary First-order Optic Effective Area results for the HRMA-MEG (top) and HRMA-HEG (bottom) at XRCF. These plots represent the automated application of the simplified Equation (10) to 132 fixed-energy data sets from Phase I. In future, "line-fraction" corrections need to be applied (as in Equation (8)) and all data need to be validated.*

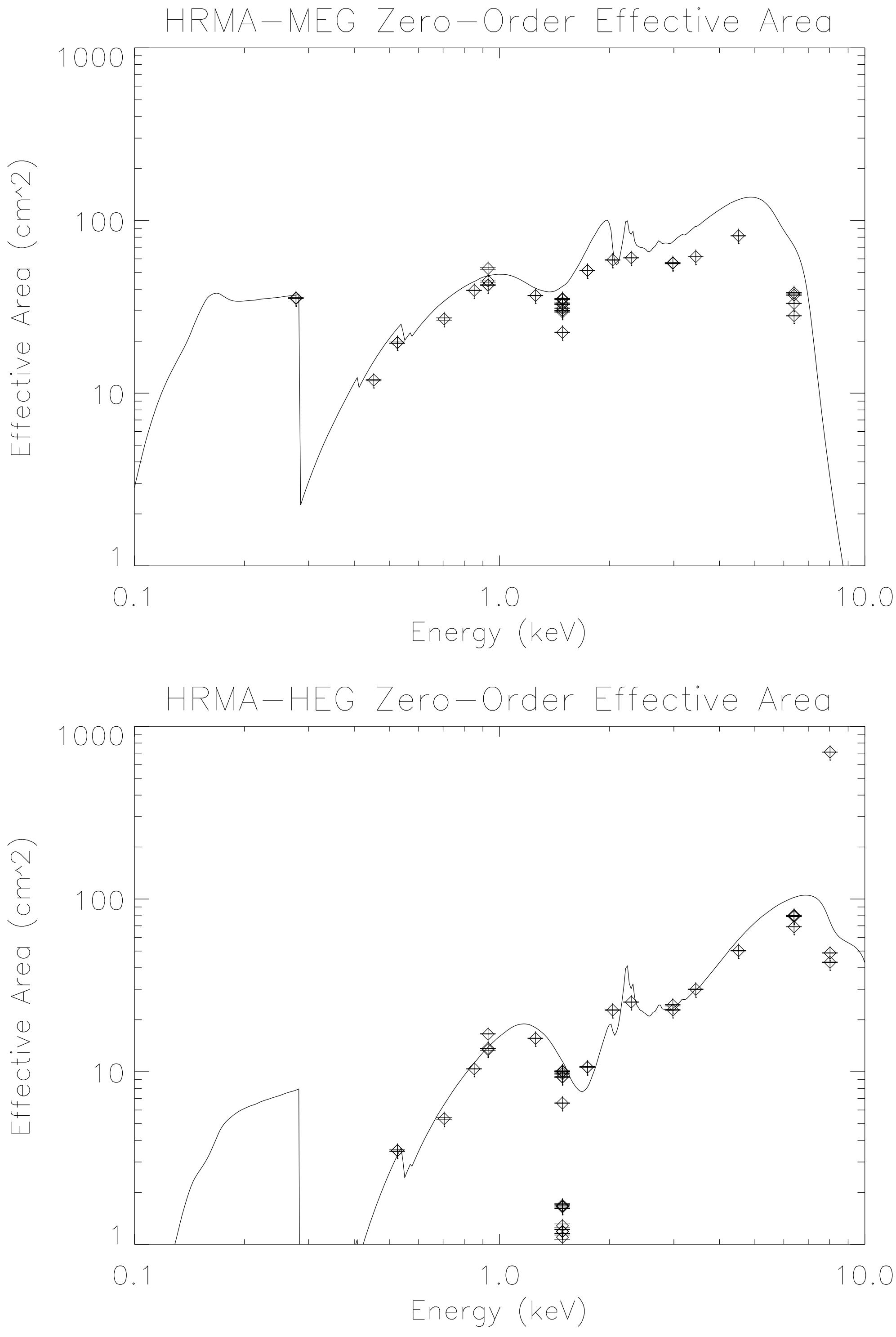

Figure 8. *Preliminary Zero-order Optic Effective Area results for the HRMA-MEG (top) and HRMA-HEG (bottom) at XRCF. These plots represent the automated analysis of 88 fixed-energy data sets from Phase I. Because the zero-order is not dispersed, the effect of ignoring "line-fraction" corrections is not as severe as in the first-order case.*

7.2. DCM-HETG-HRC-I Efficiency Ratio

That the XRCF data will support a 3% relative and 10% absolute HETGS calibration is better domonstrated with a DCM-HETG-HRC data set, Figure 9. Here, the DCM was tuned to energies in the 1.5 to 7 keV range. At each energy the ratio of counts detected in the HEG and MEG plus-first orders to the counts detected in the combined HEG and MEG zero order was computed. This ratio depends primarily on the HETG zero-order and first-order efficiencies and secondarily on the HRMA effective areas and the HRC-I spatial uniformity:

$$\frac{\mathrm{First-orders}}{\mathrm{Zero-order}}(E) = \frac{QE_{\mathrm{HRC}}(E,\vec{X_M})\sum_{s=1,3} A_s(E)\ \nu_s\ G_s(E,1) \quad + \quad QE_{\mathrm{HRC}}(E,\vec{X_H})\sum_{s=4,6} A_s(E)\ \nu_s\ G_s(E,1)}{QE_{\mathrm{HRC}}(E,\vec{X}_0)\sum_{s=1,3,4,6} A_s(E)\ \nu_s\ G_s(E,0)} \tag{11}$$

where $QE_{\mathrm{HRC}}(E,\vec{X}_*)$ is the quantum efficiency of the HRC-I at the different detected spatial regions (MEG 1st, HEG 1st, and zero orders) and the other terms have been previously defined.

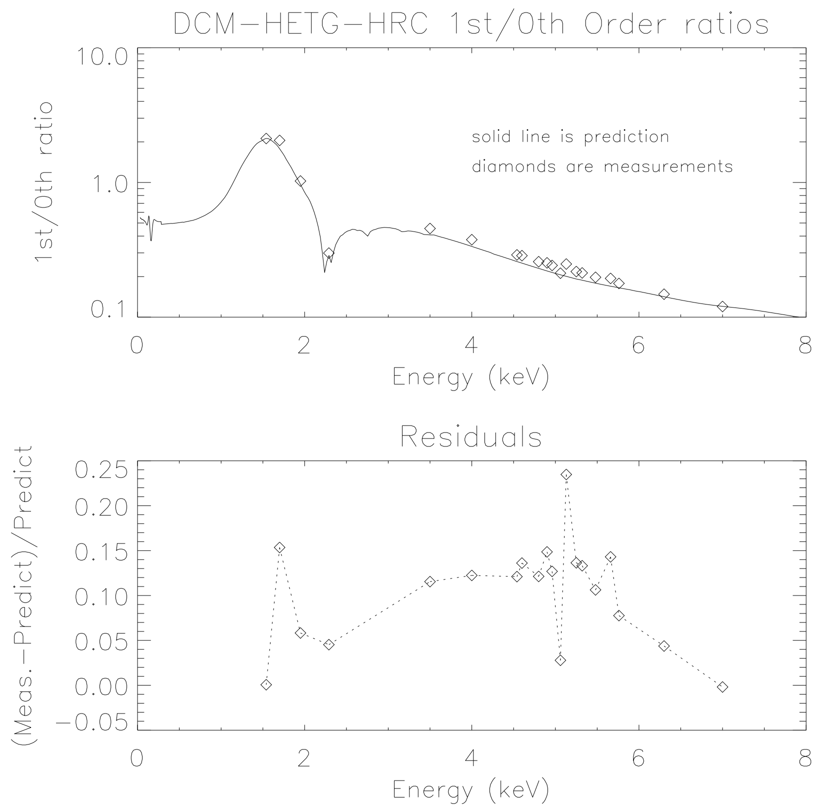

Figure 9. *DCM-HETG-HRC data: ratio of first orders to zero-order.*

7.3. HETGS Molecular Contamination Result

The quasi-monochromatic energy measurements, *e.g.*, Figure 7, do not provide data at *all* energies. In order to verify our detailed grating and detector spectral models and to search for unexpected spectral features, we observed a continuum source with the HETGS. This type of test is called "molecular contamination" (MC) because of its ability to detect the effects of contaminating layers in the system components. Figure 10 shows the result of the analysis of a fraction of the MC data taken with the HETGS. The modeled source spectrum, continuum from a Carbon target, is expected to be smooth and featureless in the 1 keV to 10 keV range. In fact, emission lines due to trace contaminants on the source anode, *e.g.*, Al-K and W-M, are visible. With the full set of data we will be able to assess our knowledge of the relative effective area calibration of the HETGS.

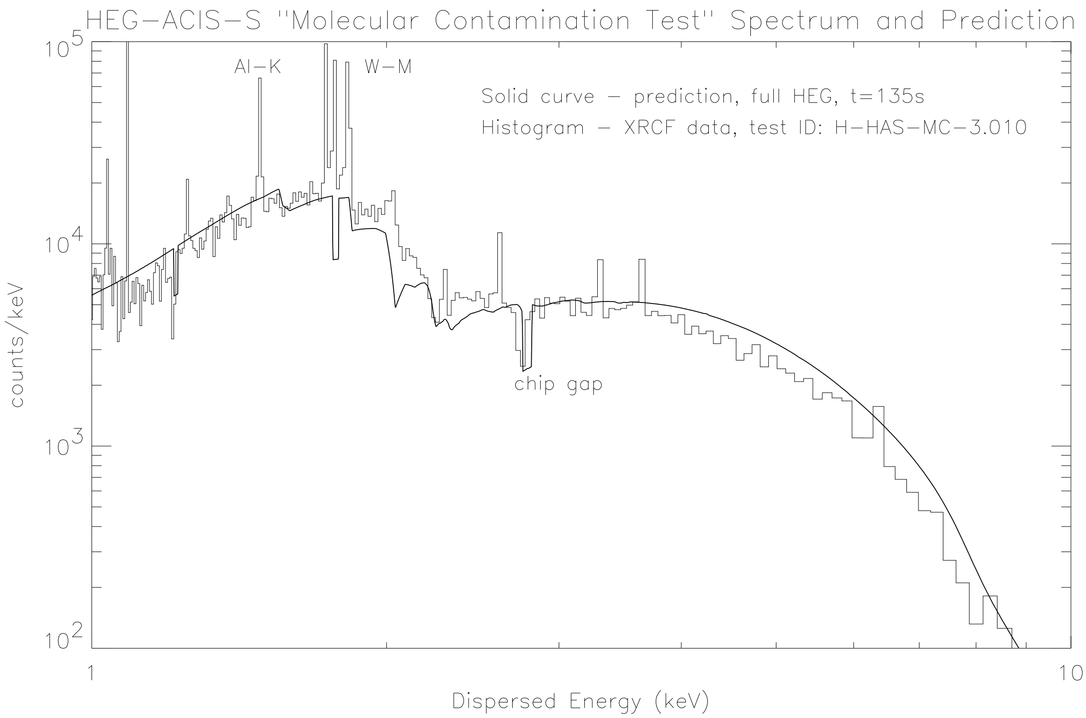

Figure 10. *Molecular contamination data and prediction. An HEG-ACIS-S spectrum is taken with the XRCF source set to produce primarily continuum photons (C target, 15 kV). The resulting observed spectrum shows source-instrumental features. Using sub-assembly models a predicted curve is plotted where only the exposure time (normalization) and chip-gap location (aim point on the ACIS-S array) have been adjusted.*

8. MOUNTAINS OF DATA...

8.1. Next analysis steps

We have just under 400 XRCF measurements relevant to the HETGS effective area. The full and accurate analysis of all the HETG (and HETGS) calibration data is an ongoing and iterative process carried out in collaboration with other AXAF groups. The next steps and improvements for XRCF grating analysis are likely to include:

- verifying the measurement parameters, *e.g.*, the diffracted order, detector apertures, etc.
- improving the "line" fitting, *e.g.*, apply XSPEC[20] fits to all FPC and SSD histograms
- applying "line_fraction" corrections to all FPC/SSD data
- calculating grating *efficiency* as a ratio of "grating-in to grating-out" measurements to separate mirror effects from grating effects
- analyzing the scanned monochromator data sets
- analyzing HRC and ACIS(2C) grating data

8.2. Beyond XRCF Analysis

Once we have a set of XRCF effective area results, they will be sythesized with the synchrotron and sub-assembly data sets to create a set of best-estimate HETG fundamental calibration products.

Finally, the HETG and other component models must be "transferred to flight". For the HETGS effective area the largest change will likely be due to an approximately 3% increase in the HRMA shell areas, $A_s(E)$, over their XRCF values. These "transferred-to-flight" models and products should provide a very accurate starting point for AXAF flight calibration and analysis activities.

9. ACKNOWLEDGEMENTS

To the full cast and crew of XRCF testing we offer and share a hearty "Congratulations!". In particular we thank Project Science, TRW, MSFC, Buddy Randolph, EK, MST, the AXAF Science Center (especially the CMDB guys and Anastasia Alexov), and the ACIS and HRC teams.

We additionally acknowledge the efforts of Mike McGuirk, Pat Hindle, Dick Elder, Chris Pak, Rich Aucoin, Ed Warren, and Bob Laliberte to get HETG to XRCF as well as providing understanding of HETG-XRCF alignments and data. Thanks to Kim Farrell for providing travel and lodging assistance for the XRCF treks.

This work was supported in part by NASA under the HETG contract NAS-38249 and the AXAF Science Center contract to the Smithsonian Astrophysical Observatory, NAS8-39073.

REFERENCES

1. A.C. Brinkman, C.J.Th. Gunsing, J.S. Kaastra, H. Bräuninger, G. Hartner, P. Predehl, J.J. Drake, J.Z. Juda, M. Juda, D. Dewey, K.A. Flanagan, and H.L. Marshall, "Preliminary Test Results on Spectral Resolution of the Low Energy Transmission Grating Spectrometer on board of AXAF", , *these proceedings*,(1997).
2. P. Predehl, H. Bräuninger, A.C. Brinkman, D. Dewey, J.J. Drake, K.A. Flanagan, C.J.Th. Gunsing, G. Hartner, J.Z. Juda, M. Juda, J. Kaastra, H.L. Marshall, and D. Swartz, "X-Ray Calibration of the AXAF Low Energy Transmission Grating Spectrometer: Effective Area",*these proceedings*,(1997).
3. Canizares, C.R., Schattenburg, M.L., and Smith, H.I., "The High Energy Transmission grating Spectrometer for AXAF", in *X-ray Instrumentation in Astronomy, Proc. SPIE*, Vol. **597**, 253–260 (1985).
4. T.H. Markert, C.R. Canizares, D. Dewey, M. McGuirk, C. Pak, and M.L. Schattenburg, "The High Energy Transmission Grating Spectrometer for AXAF", *EUX, X-Ray, and Gamma-Ray Instrumentation for Astronomy V*, Proc. SPIE, Vol. **2280**, 168–180 (1994).
5. Beuermann, K.P., Brauninger, H., and Trumper, J., *Applied Optics*, Vol. **17**, no. 15., 2304 (1978).
6. C. Pak and M. McGuirk, "Computer Aided Design for the High Energy Transmission Grating (HETG) Spectrometer", paper 94-4566 presented at the *AIAA Space Programs and Technologies Conference*, Huntsville, AL (1994).
7. M.L. Schattenburg, R.J. Aucoin, R.C. Fleming, I. Plotnik, J. Porter, and H.I. Smith, "Fabrication of High Energy X-ray Transmission Gratings for AXAF", *EUX, X-Ray, and Gamma-Ray Instrumentation for Astronomy V*, Proc. SPIE, Vol. **2280**, 181–190 (1994).
8. D.Dewey, D.N. Humpheries, G.Y. McLean and D.A. Moschella, "Laboratory Calibration of X-ray Transmission Diffraction Gratings", *EUX, X-Ray, and Gamma-Ray Instrumentation for Astronomy V*, Proc. SPIE, Vol. **2280**, 257–271 (1994).
9. H.L. Marshall, D. Dewey, K.A. Flanagan, C. Baluta, C.R. Canizares, D.S. Davis, J.E. Davis, T.T. Fang, D.P. Huenemoerder, J.H. Kastner, H.L. Marshall, N.S. Schulz, M.W. Wise, J.J. Drake, J.Z. Juda, M. Juda, A.C. Brinkman, C.J.Th. Gunsing, and J.S. Kaastra, G. Hartner and P. Predehl, "Towards the Calibration of the HETG LRF", *these proceedings*, (1997).
10. M. Born and E. Wolf, *Principles of Optics, Sixth Ed.*, pp. 401-414., Pergamon, New York, 1980.
11. D. Graessle, A.M. Clark, J.J. Fitch, B. Harris, D.A. Schwartz, R.L. Blake, "Reflectance calibrations of AXAF Witness Mirrors Using Synchrtron Radiation, 2-12 keV", *SPIE Proceedings* **2805**, 18 (1996)
12. C.S. Nelson, T.H. Markert, Y.S. Song, M.L. Schattenburg, K.A. Flanagan, R.L. Blake, J. Bauer, E.M. Gullikson, "Efficiency Measurements and Modelling of AXAF High Energy Transmission Gratings", *EUX, X-Ray, and Gamma-Ray Instrumentation for Astronomy V*, Proc. SPIE, Vol. **2280**, 191–203 (1994).
13. T.H. Markert, D. Dewey, J.E. Davis, K.A. Flanagan, D.E. Graessle, J.M. Bauer, C.S. Nelson, "Modeling the Diffraction Efficiencies of the AXAF High Energy Transmission Gratings", *SPIE Proceedings* **2518**, 424–437 (1995).
14. K.A. Flanagan, T.T. Fang, C. Baluta, J.E. Davis, D. Dewey, T.H. Markert, D.E. Graessle, J. Drake, J.E. Fitch, J.Z. Juda, J. Woo, S. Kraft, P. Bulicke, R. Fliegauf, F. Scholze, and G. Ulm, "Modeling the Diffraction Efficiencies of the AXAF High Energy Transmission Gratings: II", *EUX, X-Ray, and Gamma-Ray Instrumentation for Astronomy VII*, Proc. SPIE, Vol. **2808**, 650–676 (1996).
15. K.A. Flanagan, D. Dewey, L. Bordzol, "Calibration and Characterization of HETG grating elements at the MIT X-ray Grating Evaluation Facility", *SPIE Proceedings* **2518**, 438–456 (1995).

16. E.H. Anderson, A.M. Levine, and M.L. Schattenburg, "Transmission X-ray Diffraction Grating Alignment using a Photoelastic Modulator", *Applied Optics*, Vol. **27**, pp. 3522-3525 (1988).
17. B.J. Wargelin, E.M. Kellogg, W.C. McDermott, I.N. Evans, and S.A. Vitek, "AXAF Calibration: The HXDS Flow Proportional Counters", *these proceedings*, (1997).
18. I.N. Evans, E.M. Kellogg, W.C. McDermott, M.P. Ordway, J.M. Rosenberg, and B.J. Wargelin, "High Speed Imager AXAF Calibration Microchannel Plate Detector", *these proceedings*, (1997).
19. F.B.S. Paerels, J.V. Bixler, J.W. den Herder, C.J. Hailey, S.M. Kahn, and C.W. Mauche, "Modeling and Analysis of X-ray Emission Line Images Acquired with a Prototype Model of the XMM Reflection Grating Spectrometer", *X-Ray and Ultraviolet Spectroscopy and Polarimetry*, Proc. SPIE, Vol. **2283**, 107–118 (1994).
20. R.J. Edgar, E.Y. Tsiang, A. Tennant, S. Vitek, and D. Swartz, "Spectral Fitting in AXAF Calibration Detectors", *these proceedings*, (1997).
21. E.M. Kellogg *et al.*, "Absolute calibration of the AXAF telescope effective area", *these proceedings*, (1997).